Quantitative Magnetization Transfer Imaging: Validation and Analysis Tool Development

Ye Gu

Master of Engineering

Department of Biomedical Engineering

McGill University

Montreal,Quebec

April 2014

A thesis submitted to McGill University in partial fulfillment of the requirements of the degree of Master of Enginnering

DEDICATION

This thesis is dedicated to my family, ...

... to my beloved B.B., Gordie, Ayumi, Niels, Richard, ...

... and to everyone who made the Shark Tank such an awesome place.

ACKNOWLEDGEMENTS

First and foremost, I would like to thank my supervisor, Dr. G. Bruce Pike, for his continuous assistance, support, mentoring throughout this project and for being so knowledgeable on the subject matter. His insights helped me solve many issues.
I would also like to thank Dr. Nikola Stikov for initiating this project and for assisting me in almost all aspects of it. I also thank Dr. Ives Levesques, Mathieu Boudreau and Yaaseen Atchia for their collaboration in this project. A special thanks goes to Dr. Thomas Jubault for helping with the French version of the abstract.
I extend my gratitude to everyone in the lab for all their support, whether or not related to the project. Last but not least, I would like to thank McGill University and the department of Biomedical Engineering for the opportunity and facilities to make this project happen, and for the partial funding of this project.

ABSTRACT

An *on-resonance* balanced steady-state free precession technique for quantitative magnetization transfer (qMT) imaging is examined through an initial validation process against the existing "gold-standard" *off-resonance* spoiled gradient-echo model. Numerical simulation and sensitivity analysis of the analytical model are performed and confirm the reliability of the analytical model for the normal range of magnetization transfer (MT) parameters. *In vivo* comparison between balanced steady-state free precession and spoiled-gradient models show agreement between the two models. This new model is shown to be valid and promises to have advantages over the existing methods for its clinical practicality.

A user-friendly software package for qMT simulation as well as data analysis and model fitting was also developed as part of this project. The package will be released in the public domain, with the intention to become a standard tool for qMT researchers and users.

ABRÉGÉ

Au travers d'un processus de validation initiale, nous comparons une technique d'imagerie quantitative par transfert d'aimantation (qMT) basée sur une séquence « *en résonance* » en précession libre avec état d'équilibre et gradients équilibrés, à la référence communément admise que constitue le modèle « *hors-résonance* » en écho de gradient avec destruction de l'aimantation transversale résiduelle.

Nous réalisons une simulation numérique et une analyse de sensibilité du modèle analytique et confirmons ainsi la fiabilité de ce dernier dans une gamme habituelle de paramètres de transfert d'aimantation.

La comparaison in-vivo entre le modèle en état d'équilibre à précession libre et le modèle avec destruction de l'aimantation transversale résiduelle montre une cohérence. Ce nouveau modèle apparat comme valide et semble prometteur en terme d'utilisation clinique de par sa facilité d'utilisation, comparé aux méthodes existantes.

Dans le cadre de ce projet, nous avons également développé un logiciel de simulation du transfert d'aimantation quantitatif facile d'emploi, ainsi qu'un outil d'analyse des données et d'ajustement du modèle. Le logiciel est sur le point d'être

proposé dans le domaine public et nous espérons qu'il devienne un outil d'analyse standard pour les chercheurs et les utilisateurs du transfert d'aimantation quantitatif.

TABLE OF CONTENTS

LIST OF TABLES

LIST OF FIGURES

List of Abbreviations

F : fractional pool size

T_1 : spin-lattice relaxation time

T_2 : spin-spin relaxation time

$T_{1,f}, T_{2,f}$: free-pool spin-lattice and spin-spin relaxation times

$T_{1,r}, T_{2,r}$: restricted-pool spin-lattice and spin-spin relaxation times

Δ : offset frequency

k_f : forward magnetization exchange rate

bSSFP : balanced steady-state free precession

EMF : electromotive force

FID : free induction decay

FT : Fourier transform

MR : magnetic resonance

MRI : magnetic resonance imaging

MS : multiple sclerosis

MT : magnetization transfer

MTR : magnetization transfer ratio

NMR : nuclear magnetic resonance

qMT : quantitative magnetization transfer

RF : radio-frequence

ROI : region of interest

SAR : specific absorption rate

SPGR : spoiled gradient-echo

WM : white matter

Chapitre 1

Introduction

1.1 Introduction

Since its first demonstration in 1946 by Nobel Laureates E. Purcell and F. Bloch, the phenomenon of nuclear magnetic resonance (NMR) has found a multitude of applications in many scientific fields [6, 40]. The application of NMR extended to the medical field in the 1970s, when Paul Lauterbur introduced the first magnetic resonance (MR) images [22]. Since then, this non-invasive imaging method has produced a wide range of *in vivo* imaging techniques [18, 35]. In addition to providing exquisite macroscopic structural images, magnetic resonance imaging (MRI) can be sensitized to tissue microstructure by combining specific imaging techniques with models describing the signal properties. The analysis of such models can reveal, directly or indirectly, tissue microstructure or functions [24].

One important MRI technique is magnetization transfer (MT) imaging. First discovered accidentally by Balaban *et al.* in 1989, MT imaging sensitizes the MRI measurement to properties of the macromolecular component of tissue [50]. In addition to conventional imaging techniques, MT imaging is an important tool in the study of neurological diseases, notably in multiple sclerosis (MS). Many imaging techniques have been proposed for performing MT imaging, notably magnetization transfer ratio (MTR), which allows the visualization of MT effects in a semi-quantitative manner [19]. Recent studies have shown that quantitative analyses of the MT effect offer better specificity to underlying parameters of the MT mechanism, leading to a better understanding of MS pathology [13, 17, 41, 44].

While there exist multiple imaging techniques for the quantitative model describing the transfer of magnetization between protons in water and in macromolecules, two of them are of particular interest. The first one, using an *off-resonance* spoiled gradient (SPGR) pulse sequence [44], is a well validated technique that is widely accepted for quantitative magnetization transfer (qMT) imaging. The second technique is more recent and proposes an *on-resonance* balanced steady-state free precession (bSSFP) pulse sequence, which promises to provide higher resolution and better signal-to-noise ratio (SNR) [13].

This thesis focuses on these two qMT imaging techniques and consists of two main parts : 1. a comparison between the *on-resonance* and the *off-resonance* qMT imaging techniques ; and 2. development of a standard simulation and processing software toolkit for these two imaging techniques. Background information on the theories behind MRI and more specifically the two techniques of qMT imaging are presented in Chapter 2. Chapter 3 will first present the experimental methods used to compare the *on-resonance* bSSFP technique against the well-validated *off-resonance* SPGR protocol, followed by an introduction to the design concepts of the simulation/processing software package. The results of the validation as well as the final product of the software package will be presented in Chapter 4. A discussion on the significance and limitations of the results, as well as the functionality of the software package, can be found in Chapter 5. Chapter 6 will summarize the work done and will propose directions for future work.

Chapitre 2

Background

MRI technology is based on the phenomenon of NMR. NMR is a property of atomic nuclei with a non-zero spin angular momentum placed in the presence of an external magnetic field. This chapter will offer a brief introduction to the quantum mechanical description of angular momentum and spin of nuclei, while using a more classical approach to explain the NMR phenomenon. It will then explain the concept of imaging using NMR based on detailed explanations by Haacke *et al.* [18] and Nishimura [35]. Then, the mechanism of MT will be explained through a two-pool exchange model. Finally, details of the qMT imaging techniques will be outlined, putting emphasis on the *on-resonance* bSSFP method.

2.1 Basics of NMR

2.1.1 Spin and magnetic moment

If the total number of protons and neutrons of a nucleus is odd, then the nucleus has a net spin angular momentum, or *spin*, as it is more commonly referred to in quantum mechanics. The hydrogen proton (^{1}H) is the most commonly used nucleus in MRI. Other examples of nuclei used for MRI include sodium (^{23}Na), phosphorus (^{31}P), and the carbon-13 (^{13}C) isotope.

The spin of a particle is directly related to its moment of inertia I by the spin operator in quantum mechanics :

$$\mathbf{S} = \hbar I, \tag{2.1}$$

where $\hbar$ is Planck's constant. Any nucleus with a net angular momentum can be modelled by a magnetic dipole with magnetic dipole moment μ given by :

$$\mu = \gamma \mathbf{S}, \tag{2.2}$$

where γ is the gyromagnetic ratio, a known constant for a given species. For hydrogen protons, $\gamma/2\pi = 42.58$MHz/Tesla.

2.1.2 Thermal equilibrium

When a magnetic dipole is placed in an external magnetic field $\mathbf{B} = B_0\hat{\mathbf{z}}$, the magnetic moment of this dipole - originally oriented randomly - tends to align with the field, either parallel (n_+) or anti-parallel (n_-). These two alignments represent the two possible energy states which a particle can occupy in this situation. For a proton, which has spin $\pm 1/2$, the energy difference between these two states is given by :

$$\Delta E = \hbar\gamma B_0. \tag{2.3}$$

The numbers of nuclei in a given sample occupying each state at a given temperature T can be described using the Boltzmann distribution :

$$\frac{n_-}{n_+} = e^{-\Delta E/kT}, \tag{2.4}$$

where k is the Boltzmann constant. An excess of spins, on the order of parts-per-million, will occupy the low-energy state, resulting in a net nuclear magnetization M of the given sample, which, at thermal equilibrium is aligned with the external magnetic field.

2.1.3 Precession

From a classical standpoint, if a magnetic dipole is placed in a magnetic field $\mathbf{B}$, it experiences a torque τ, which represents the rate of change of the spin angular momentum :

$$\tau = \frac{d\mathbf{S}}{dt} = \mu \times \mathbf{B}. \tag{2.5}$$

From equation 2.2, we get :

$$\frac{d\mu}{dt} = \mu \times \gamma\mathbf{B}. \tag{2.6}$$

From a macroscopic point of view, summing over the entire sample, $\mathbf{M} = \Sigma\mu$, yields :

$$\frac{d\mathbf{M}}{dt} = \mathbf{M} \times \gamma\mathbf{B}. \tag{2.7}$$

The solution of this differential equation describes a precession about the direction of the external field $\mathbf{B}$. The resonance frequency of the precession is called the Larmor frequency, and is given by the Larmor equation :

$$\omega_0 = \gamma B_0[\text{rad/s}]. \tag{2.8}$$

For the hydrogen proton and for magnetic field strengths typically used in imaging (0.1-10T), ω_0 is in the radio-frequency (RF) range of the frequency spectrum.

2.1.4 Excitation

An extra RF field $\mathbf{B}_1$ can be applied to excite the magnetization $\mathbf{M}$. Ideally, this field is circularly polarized : :

$$\mathbf{B}_1 = B_1 \left[\hat{\mathbf{x}} \cos(\omega t) - \hat{\mathbf{y}} \sin(\omega t)\right]. \tag{2.9}$$

This field excites the magnetization and rotates it away from its original longitudinal alignment, as shown in the left part of Fig. 2–1. When $\omega = \omega_0$, the $\mathbf{B}_1$ field is *on-resonance* and achieves the optimal energy deposition. If the $\mathbf{B}_1$ is linearly polarized, it can be decomposed into two circularly polarized fields in opposite orientations and achieve the same result, but less efficiently.

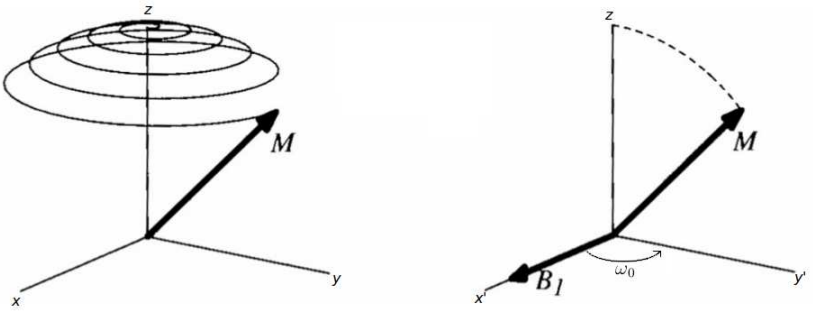

FIGURE 2–1: RF Excitation : illustration of **M** getting tilted away from the longitudinal axis in the lab reference frame (left), and a frame rotating at a frequency equal to the Larmor frequency (right) (adapted from [35]).

The actual motion of the precessing magnetization vector can be greatly simplified in a reference frame (x', y', z) rotating about the $z-$axis, as shown in the right part of Fig. 2–1.

An RF excitation pulse with amplitude B_1 will result in a rotation of the magnetization vector about the $x'-$axis at an angular frequency :

$$\omega_1 = \gamma B_1. \tag{2.10}$$

ω_1 is called the nutation frequency. An arbitrarily shaped RF excitation pulse $\omega_1(t)$ with a duration T_{RF} will then cause the magnetization vector to rotate a net *flip angle* of [21] :

$$\alpha = \int_0^{\mathrm{T}_{RF}} \omega_1(t)dt. \tag{2.11}$$

After the magnetization is tilted away from the longitudinal $z-$ axis, its precession generates a change in the magnetic flux Φ in the receiving coils and thereby induces an electromotive force (EMF), according to Faraday's law of induction :

$$\mathrm{EMF} = -\frac{\partial \Phi}{\partial t}. \tag{2.12}$$

An electric signal, commonly referred to as free induction decay (FID) can then be detected for imaging.

2.1.5 Relaxation

Once the RF pulse creating a rotational magnetic field $\mathbf{B}_1$ tilts the magnetization vector $\mathbf{M}$ into the transverse $xy-$plane, the magnetization goes into precession and relaxes. In other words, the magnetization in the $xy-$plane disappears and the magnetization in the $z-$direction recovers to its original value M_0. The longitudinal component recovers with a spin-lattice relaxation time constant T_1, with a mechanism described by :

$$\frac{dM_z(t)}{dt} = -\frac{M_z(t) - M_0}{T_1}. \tag{2.13}$$

The solution of equation 2.13 is :

$$M_z(t) = M_0 + (M_z(t_0) - M_0)e^{-\frac{t}{T_1}}. \tag{2.14}$$

The transverse component of the magnetization, on the other hand, disappears in the $xy-$plane with a spin-spin relaxation time constant T_2. This transverse relaxation can be described as follows :

$$\frac{dM_{xy}(t)}{dt} = -\frac{M_{xy}(t)}{T_2}, \tag{2.15}$$

with solution :

$$M_{xy}(t) = M_{xy}(t_0)e^{-\frac{t}{T_2}}. \tag{2.16}$$

Typical values of T_1 are on the order of seconds, which is considered long in the context of MRI. The values of T_2 differ largely between the protons in free water

molecules and protons bound to macromolecules, such as lipids. At magnetic field strengths of 1.5T to 3T, typical values of T_2 free water molecules ranges between 50 to 100ms, whereas T_2 of those in macromolecules are usually on the order of 10 to 50μs. The relaxation time constants can also be expressed as relaxation rates $R_1 = \frac{1}{T_1}$ and $R_2 = \frac{1}{T_2}$ [15].

2.1.6 Bloch equation

Combining the effects of precession and relaxation, the behaviour of the magnetization vector $\mathbf{M}$ can be described by the Bloch equation [6], in vector form :

$$\frac{d\mathbf{M}(t)}{dt} = \mathbf{M}(t) \times \gamma\mathbf{B} - \frac{M_x(t)\hat{\mathbf{x}} + M_y(t)\hat{\mathbf{y}}}{T_2} - \frac{(M_z(t) - M_0)\hat{\mathbf{z}}}{T_1}. \tag{2.17}$$

2.2 Imaging

Since the FID signal comes from the entire sample, it is not possible to localize it if the entire sample precesses at the same frequency. In order to spatially resolve it, *gradient* magnetic fields are applied in addition to the main static field. This allows the field strength - and thereby the resonance frequency - to vary spatially. The received signal then consists of a range of frequencies and can be mapped,

using the Fourier transform (FT), to a range of spatial components, thereby achieving spatial resolution.

Given a time-varying gradient field

$$\Delta B(\mathbf{r}, t) = \mathbf{G}(t) \cdot \mathbf{r} \tag{2.18}$$

and a static field B_0, as is common in MRI, we have a non-uniform magnetic field :

$$\mathbf{B}(\mathbf{r}, t) = [B_0 + \Delta B(\mathbf{r}, t)]\, \hat{\mathbf{z}}. \tag{2.19}$$

The Bloch equation during the free precession phase can then be generalized to :

$$\frac{d\mathbf{M}(t)}{dt} = \left(\frac{1}{T_2(\mathbf{r})} + i\left[\omega_0 + \gamma \mathbf{G}(t) \cdot \mathbf{r}\right] \right) \mathbf{M}(t), \tag{2.20}$$

where $\omega_0 = \gamma B_0$. Since only the $xy-$component of the magnetization is used for imaging, equation 2.20 has the solution :

$$M_{xy}(\mathbf{r}, t) = M_{xy,0}(\mathbf{r}) e^{-\frac{t}{T_2(\mathbf{r})}} e^{-i\omega_0 t} e^{-i\gamma \int_0^t \mathbf{G}(\tau)\cdot\mathbf{r} d\tau}. \tag{2.21}$$

Now for simplicity, assuming that the T_2 decay is negligible over the sampling interval and that the received signal is demodulated in frequency by ω_0 using phase sensitive detection, the terms $e^{-i\omega_0 t}$ and $e^{-\frac{t}{T_2(\mathbf{r})}}$ can be dropped. Assuming a 2-D object with magnetization $m(x, y)$ (after integration over one slice in the slice direction), the signal can be written as :

$$s(t) = \int_x \int_y m(x, y) e^{-i2\pi[k_x(t)x + k_y(t)y]} dx\, dy, \tag{2.22}$$

where

$$\begin{aligned} k_x(t) &= \frac{\gamma}{2\pi} \int_0^t G_x(\tau) d\tau \\ k_y(t) &= \frac{\gamma}{2\pi} \int_0^t G_y(\tau) d\tau \end{aligned} \tag{2.23}$$

are the time integrals of the gradient waveforms. By inspection, equation 2.22 is in the exact form of the Fourier transform of $m(x, y)$, i.e. :

$$s(t) = \mathcal{M}\left(k_x(t), k_y(t)\right). \tag{2.24}$$

This leads to the realization that at any given time, the detected signal is the FT of the magnetization at some spatial frequency. The inverse FT can then be used to reconstruct the image of the object.

2.3 Magnetization Transfer

2.3.1 Myelin and WM pathology

Brain tissue can be divided into white matter (WM) and grey matter (GM). GM is mainly composed of neuronal somata, whereas myelinated axons and glial cells are the main components of WM. WM accounts for a large portion of the brain tissue and are generally present in the form of axon bundles. These bundles serve as connections between GM areas and allow communication between different areas of the brain.

An important component of WM axons is myelin, which wraps around the axons in the form of a myelin sheath, as shown in Fig. 2–2. Myelin electrically insulates the axons and plays an important role in enabling faster conduction of *action potentials* along the axon [36].

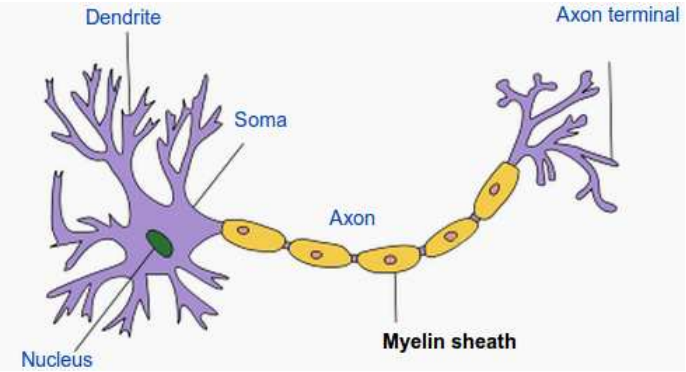

FIGURE 2–2: Illustration of a typical neuron, showing the myelin sheath wrapping around the axon.

The myelin sheath can be damaged by injury, toxins and neurological diseases such as Alzheimer's disease and multiple sclerosis (MS). These damages can greatly affect the functions of the brain by reducing the conduction speed and causing atrophy [23]. The qMT imaging techniques presented in this thesis provide biomarkers specific to the amount of myelin in tissue.

2.3.2 Macro-molecular structures and absorption *lineshape*

Hydrogen protons can be found in a multitude of different environments and therefore have different behaviour to consider in NMR. However, they can be categorized into two general environments as shown in Fig. 2–3.

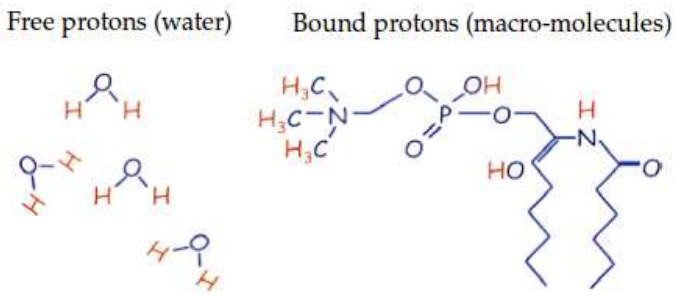

FIGURE 2–3: Illustration of the two general environments in which hydrogen protons are found (from [48]).

The first one, which includes the majority of hydrogen protons, is the group of small and mobile molecules, most importantly water. These *free* protons have relatively longer T_2 values (denoted by $T_{2,f}$), ranging between 50 to 100ms. These protons also have a very narrow absorption *lineshape*, as shown in Fig. 2–4.

The *lineshape* of a molecule is the FT of the decay curve, and represents the distribution of the relative strength of resonance as a function of frequency offset Δ. The *free* protons have a *Lorentzian lineshape* with width $\frac{1}{T_2}$, which corresponds to the exponential decay in the time domain. This very narrow *lineshape* means that these *free* protons can only be excited with frequencies very close to the Larmor frequency.

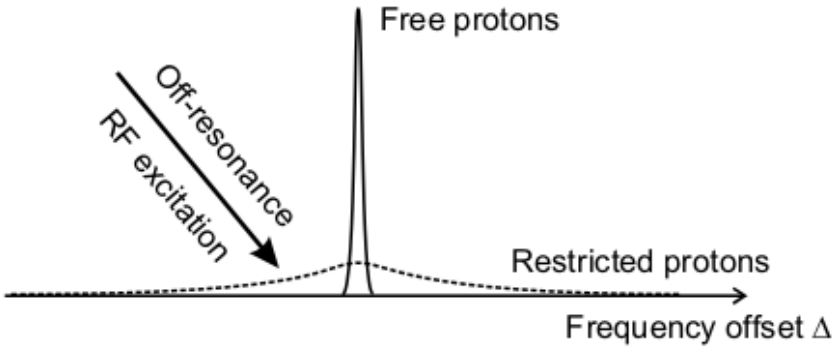

FIGURE 2–4: Graphical representation of the absorption *lineshapes* of the *free* and the *restricted* protons (from [14]).

The second environment in which hydrogen protons are found is the group of *semi-solid* macromolecules, such as myelin. These protons have very short T_2 values (denoted by $T_{2,r}$), on the order of 10μs. This short relaxation time makes it very difficult to directly image these *bound*, or *restricted*, protons on clinical MRI systems. On the other hand, the *lineshape* of the *restricted* protons is much broader, meaning they can be easily saturated *off-resonance*, as shown in Fig. 2–4. The *lineshape* of the macro-molecules is modelled by a *Super-Lorentzian*, as is often done in literature [15, 44].

$$G(\Delta) = \int_0^1 \sqrt{\frac{2}{\pi}} \frac{T_{2,r}}{|3u^2 - 1|} exp\left[-2\left(\frac{2\pi\Delta T_{2,r}}{3u^2 - 1}\right)^2\right] \mathrm{d}u. \tag{2.25}$$

The *Super-Lorentzian* $G(\Delta)$ diverges at $\Delta = 0$. For *on-resonance* excitations, the value of the absorption rate is interpolated [15].

2.3.3 Magnetization Transfer and the Two-Pool Exchange Model

First presented by McConnell in 1958 [32] and further analyzed by Edzes and Samulski [10], Wu [51] and Henkelman et al. [20], the MT phenomenon describes the exchange of magnetization between mobile protons in water molecules and protons bound in macromolecules by nuclear dipole coupling. This phenomenon can be described using a two-pool cross-relaxation/exchange model.

The two-pool model reflects the coupling between the macromolecular protons in the *restricted pool* and the mobile protons in the *free pool*, allowing the magnetization of the *restricted pool* to influence that of the *free pool*. As shown in Fig. 2–5, the magnetization exchange between the two pools is determined by a fundamental rate constant R [19]. Using R, two pseudo-first-order rate constants $k_f = RM_{0,r}$ and $k_r = RM_{0,f}$ can be derived to describe respectively the rate of magnetization transfer from the free pool to the restricted pool and vice-versa. $M_{0,f}$ and $M_{0,r}$ denote the equilibrium magnetization of the free and restricted pool, respectively, as shown by the sizes of the two boxes in Fig. 2–5. The fractional size of the restricted pool with respect to the free pool is then $F = \frac{M_{0,r}}{M_{0,f}} = \frac{k_f}{k_r}$ [15]. This

parameter F has been shown to correlate with the myelin content in WM [24, 14].

For simplicity, $M_{0,f}$ is normalized to 1 most of the time.

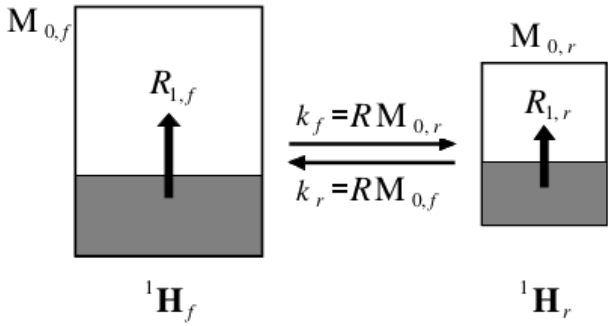

FIGURE 2–5: Schematic illustration of the Two-pool model with respective relaxation rates $R_{1,f}$ and $R_{1,r}$. Saturation level of each pool is illustrated by the size of shaded area (adapted from [11]).

This two-pool model can be formulated mathematically as a modified version of the Bloch equations including exchange of magnetization [17, 44].

$$\frac{dM_{x,f}}{dt} = -R_{2,f}M_{x,f} - \Delta M_{y,f} \tag{2.26a}$$

$$\frac{dM_{y,f}}{dt} = -R_{2,f}M_{y,f} + \omega_1(t)M_{z,f} + \Delta M_{x,f} \tag{2.26b}$$

$$\frac{dM_{z,f}}{dt} = R_{1,f}(M_{0,f} - M_{z,r}) - k_f M_{z,f} + k_r M_{z,r} - \omega_1(t)M_{y,f} \tag{2.26c}$$

$$\frac{dM_{z,r}}{dt} = R_{1,r}(M_{0,r} - Mz,r) + k_f M_{z,f} - k_r M_{z,r} - W(\Delta,t)M_{z,r}, \tag{2.26d}$$

where $\omega_1(t) = \gamma|\mathbf{B}_1(t)|$ depends on the shape of the excitation pulse. The $W(\Delta, t)$ in equation 2.26d is the absorption rate and is defined as [44] :

$$W(\Delta, t) = \pi\omega_1^2(t)G(\Delta), \tag{2.27}$$

where $G(\Delta)$ is the absorption *lineshape* of the restricted pool.

2.4 qMT imaging techniques for the two-pool model

Two main imaging techniques are of particular interest for this thesis. The first one is an *off-resonance* SPGR imaging protocol developed by Sled and Pike [44] and optimized by Levesque *et al.* [29]. The second one is an *on-resonance* bSSFP protocol proposed by Gloor *et al.* [15]. The former is well-validated, well-documented and considered the "gold standard" for quantitative MT imaging, whereas the latter is a new method that promises to offer higher resolution, better signal-to-noise ratio and a clinically feasible scan time. While this section will provide a overview of both methods, more emphasis will be made on the new *on-resonance* bSSFP method, by providing more mathematical details.

2.4.1 qMT imaging using *off-resonance* spoiled gradient-echo method

The main idea of the *off-resonance* SPGR imaging method is to saturate the *restricted* pool alone using an *off-resonance* MT pulse, which is possible because the *free* pool has a very narrow *lineshape*. Exchange of magnetization happens between the *restricted* pool and the *free* pool due to cross-relaxation. The magnetization saturation is "transferred" to the free pool. An *on-resonance* excitation pulse is then applied with gradients for spatial encoding, as shown in Fig. 2–6. The typical TR of this sequence is about 50ms, as it is previously found to be the optimal value for distinguishing myelin and water based on their respective $T2$ values [24].

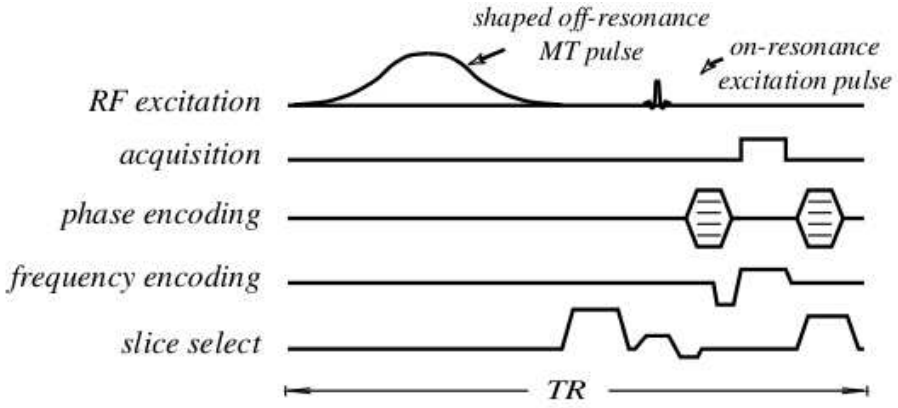

FIGURE 2–6: Illustration of the spoiled gradient-echo pulse sequence with MT saturation (from [43]).

The behaviour of the magnetization depends on the saturation power and offset frequency of the MT saturation pulse. Model parameter estimation can be

achieved by acquiring a set of MT-weighted images using different saturation powers and/or offset frequencies and fitting the results to a model. Different protocols, with numbers of MT-weighted images ranging from 4 to 60, have been proposed [24]. In the current study, we made use of a protocol that has been optimized by Levesque *et al.* [29] to acquire only 10 MT-weighted images.

2.4.2 Analytical solution of the *off-resonance* qMT-SPGR

The behaviour of the magnetization, and thereby the signal detected, can be modelled by numerically simulating each step of this pulse sequence using the Bloch equations 2.26a through 2.26d. However, this process is very time consuming. Sled and Pike have proposed a rectangular pulse model of steady-state pulsed MT [43] to decompose and approximate the effect of shaped *off-resonance* RF pulses, as shown in Fig. 2–7. This model reduces the *off-resonance* effect on the *free* pool to an instantaneous saturation and neglects the *on-resonance* effect on the *restricted* pool. Each sequence is decomposed into periods of free-precession, instantaneous saturation, and *off-resonance* continuous wave irradiation. This model is shown to accurately approximate the real MT effect and allows the derivation of an analytical solution and thereby a much faster estimation of the signal behaviour [43].

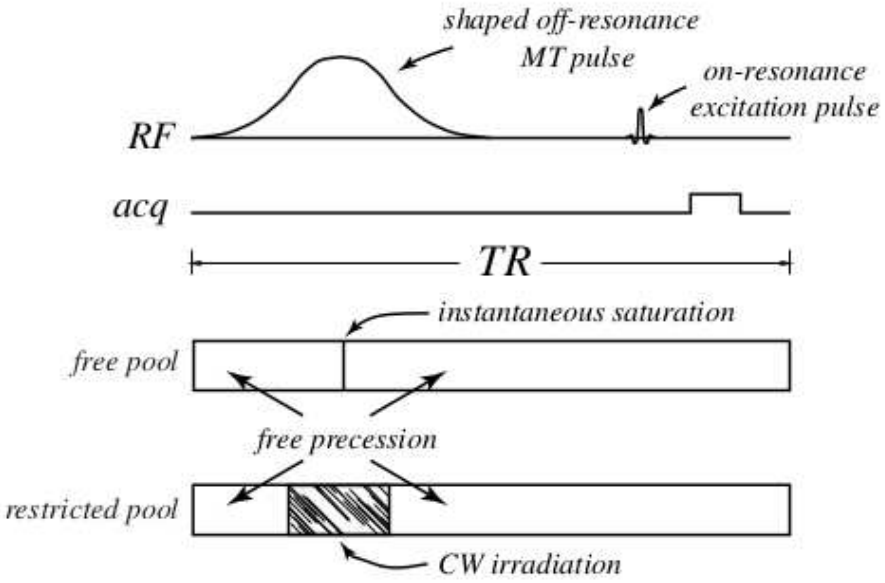

FIGURE 2–7: Decomposition of the *off-resonance* MT-SPGR sequence into periods of free precession, instantaneous *on-resonance* free pool saturation, and continuous wave *off-resonance* restricted pool saturation (from [43]).

The analytical solution derived from this approximation can be expressed as

follows :

$$M_{xy,f} = \frac{c(E_1 - 1)(E_2 - 1)(\lambda_2 - \lambda_1)S_{1,f}M_{z,f}^{SS}\sin\theta}{(E_1 - 1)(S_f E_2 - 1)(\lambda_2 - \lambda_1) + (S_f - 1)(E_2 - E_1)(\lambda_2 - R_{1,f} - k_f)}, \quad (2.28)$$

where

$$\lambda_{1,2} = \frac{1}{2}(R_{1,f} + k_f + R_{1,r} + k_r + W) \pm \frac{1}{2}\sqrt{\begin{array}{l}(R_{1,f} + k_f + R_{1,r} + k_r + W)^2 \\ \\ -4(R_{1,f}R_{1,r} + k_f R_{1,r} + R_{1,f}k_r + R_{1,f}W + k_f W)\end{array}},$$

with $E_1 = \exp(-\lambda_1 t)$ and $E_2 = \exp(-\lambda_2 t)$. θ is the *flip angle* of the excitation pulse and c is a constant accounting for other factors such as proton density and equipment sensitivity [43].

2.4.3 qMT imaging using *on-resonance* bSSFP

The *on-resonance* bSSFP method takes a different approach towards achieving quantitative MT analysis. The *free* and *restricted* pools are excited simultaneously using a balanced SSFP-FID sequence with low *flip angles* of very short duration, alternating in the $\pm x'-$ direction every TR, until a dynamic steady-state is reached. Imaging gradients are then applied and signal acquired, as shown in Fig. 2–8. Typical TR of this *on-resonance* bSSFP sequence is 3 to 5 ms.

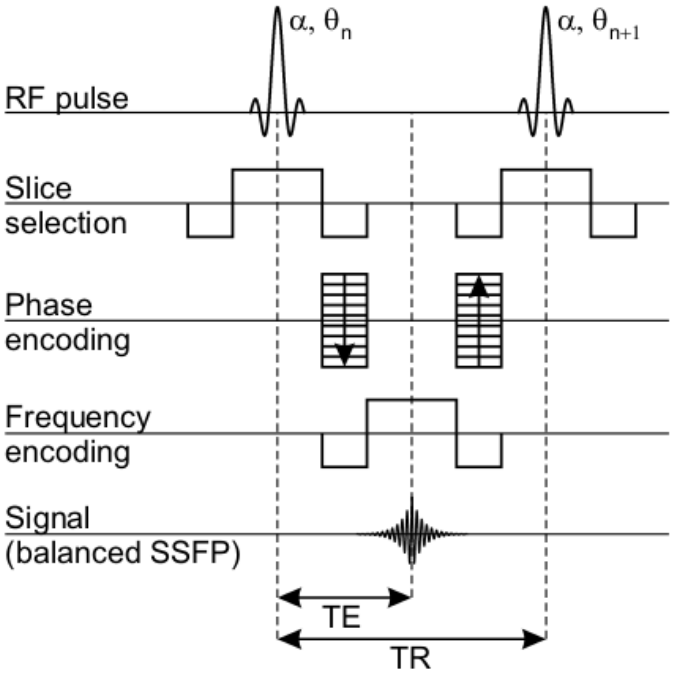

FIGURE 2–8: Illustration of a typical *on-resonance* bSSFP pulse sequence (from [14]).

Since there is no *off-resonance* pulse, offset frequencies and *off-resonance* pulse power are irrelevant in this method. The actual signal stength depends on a combination of TR, *flip angle* and *on-resonance* excitation pulse duration (T_{RF}). Again, by acquiring a set of MT-weighted images using different combinations of these sequence parameters, the data can be fitted to a model to determine the MT parameters. More specifically, 8 to 10 data sets by varying the flip angle and 6 to 8 data sets by varying the the TR are combined together to get a well-conditioned fit.

Since the bSSFP method uses *on-resonance* excitation pulses, the Bloch equations 2.26a - 2.26d are further simplified by eliminating terms involving frequency offset. The set of equations then reduces to [15] :

$$\frac{dM_{x,f}}{dt} = -R_{2,f}M_{x,f}, \tag{2.29a}$$

$$\frac{dM_{y,f}}{dt} = -R_{2,f}M_{y,f} + \omega_1(t)M_{z,f}, \tag{2.29b}$$

$$\frac{dM_{z,f}}{dt} = R_{1,f}(M_{0,f} - M_{z,r}) - k_f M_{z,f} + k_r M_{z,r}, -\omega_1(t)M_{y,f} \tag{2.29c}$$

$$\frac{dM_{z,r}}{dt} = R_{1,r}(M_{0,r} - Mz, r) + k_f M_{z,f} - k_r M_{z,r} - W(\Delta \to 0, t)M_{z,r} \tag{2.29d}$$

2.4.4 Analytical solution of the *on-resonance* bSSFP model

Starting with the simplified Bloch equations 2.29a - 2.29d, an analytical solution for steady-state can be found by solving the relaxation, the exchange and the excitation terms separately and combining the results.

Assuming, without loss of generality, that the excitation pulse is always applied along the $x-$axis, Eq. 2.29a can be eliminated for the initial condition $M_{0_x,f} = 0$. The system reduces to $\mathbf{M} = (M_{y,f}, M_{z,f}, M_{z,r})$. The relaxation, exchange and excitation parts are then solved separately.

The relaxation part is just a set of three non-coupled first-order ODEs, each having an exponential decay as solution. Expressing the solutions in matrix form yields the solution $\mathbf{M}(t) = \mathbf{E}(t) \cdot \mathbf{M}(\mathbf{0})$, with

$$\mathbf{E}(t) = \begin{pmatrix} E_{2,f} & 0 & 0 \\ 0 & E_{1,f} & 0 \\ 0 & 0 & E_{1,r} \end{pmatrix} \equiv \begin{pmatrix} e^{-R_{2,f}t} & 0 & 0 \\ 0 & e^{-R_{1,f}t} & 0 \\ 0 & 0 & e^{-R_{1,r}t} \end{pmatrix}. \tag{2.30}$$

For the exchange part, $M_{z,f}$ and $M_{z,r}$ are coupled, whereas $M_{y,f}$ does not have an exchange term. The coupled equations can be solved either by a standard 2-by-2 eigenvalue method or by using the matrix exponential. Substituting $k_f = k_r F$, the solution can be expressed as $\mathbf{M}(t) = \mathbf{A}(t) \cdot \mathbf{M}(\mathbf{0})$, with

$$\mathbf{A}(t) = \frac{1}{F+1} \begin{pmatrix} F+1 & 0 & 0 \\ 0 & 1+Fe^{-(F+1)k_r} & 1-e^{-(F+1)k_r} \\ 0 & F-Fe^{-(F+1)k_r} & F+e^{-(F+1)k_r} \end{pmatrix}. \tag{2.31}$$

To solve the excitation part, an instantaneous saturation is assumed. For the free pool, an excitation pulse simply results in a rotation by an angle α of the magnetization vector in the $y'z-$plane in the rotational frame. For the restricted pool, an excitation pulse causes a saturation. Thus the solution, in matrix form, is expressed as $\mathbf{M}(t) = \mathbf{R}_{\mathbf{x}}(\alpha, t) \cdot \mathbf{M}(0)$, with

$$\mathbf{R_x}(t) = \begin{pmatrix} \cos\alpha & \sin\alpha & 0 \\ -\sin\alpha & \cos\alpha & 0 \\ 0 & 0 & e^{-\langle W(\Delta\to 0)\rangle t} \end{pmatrix}. \tag{2.32}$$

Finally, the effect of pulse alternation can be mathematically expressed by an instantaneous rotation of the x' and y' components of the magnetization vector by 180° before the excitation takes place. Since only the magnitude of the magnetization vector is considered, the effect of rotating the entire frame by 180° is the same as applying alternating pulses. In matrix form,

$$\mathbf{R_z}(t) = \begin{pmatrix} -1 & 0 & 0 \\ 0 & -1 & 0 \\ 0 & 0 & 1 \end{pmatrix}. \tag{2.33}$$

Now the effects of each part can be combined together and steady-state solutions can be derived following standard methods [18]. Assuming that relaxation takes place before exchange, the magnetization $\mathbf{M_n}$ immediately before the nth excitation pulse can be expressed by applying the excitation, the relaxation, the exchange and finally the axis-rotation matrices on the magnetization $\mathbf{M_{n-1}}$ immediately before the n-1th pulse. Mathematically it can be expressed as

$$\mathbf{M_n} = \mathbf{R_z A}(\mathbf{E R_x M_{n-1}} + \mathbf{M_0}), \text{ where } \mathbf{M_0} = \begin{pmatrix} 0 \\ M_{0,f}(1 - E_{1,f}) \\ M_{0,r}(1 - E_{1,r}) \end{pmatrix}. \tag{2.34}$$

At steady-state, $\mathbf{M_n} = \mathbf{M_{n-1}}$, so the magnetization $\mathbf{M}_\infty$ at steady-state is then

$$\mathbf{M}_\infty = (\mathbf{I} - \mathbf{R_z A E R_x})^{-1} \mathbf{A M_0}. \tag{2.35}$$

Applying the excitation pulse once again we have the steady-state magnetization $\mathbf{M}$ right after a pulse :

$$\mathbf{M} = \mathbf{R_x}(\mathbf{I} - \mathbf{R_z A E R_x})^{-1} \mathbf{A M_0}. \tag{2.36}$$

Computing the $y-$component of this vector, with the assumption that $M_{0,f} = 1$, we get the required results shown in equation 2.37[15]

$$M_y^+ = M_{0,f} \sin\alpha \frac{(1 - E_{1,f})B + C}{A - BE_{1,f}E_{2,f} - (BE_{1,f} - AE_{2,f})\cos\alpha} \tag{2.37}$$

where

$$\begin{aligned} A &= 1 + F - f_w E_{1,r}(F + f_k), \\ B &= 1 + f_k(F - f_w E_{1,r}(F + 1)), \\ C &= F(1 - E_{1,r})(1 - f_k), \\ f_k &= \exp[-(k_f + k_r)\mathrm{TR}], \\ f_w &= \exp[-\langle W(\Delta \to 0)\rangle \, \mathrm{T}_{RF}], \\ E_{2,f} &= \exp(-R_{2,f}\mathrm{TR}), \\ E_{1,f} &= \exp(-R_{1,f}\mathrm{TR}), \\ E_{1,r} &= \exp(-R_{1,r}\mathrm{TR}), \end{aligned} \tag{2.38}$$

In Eq.2.37, the *flip angle* α, the pulse duration T_{RF} and the repetition time between two pulses TR are properties of the excitation pulse, thus controlled variables. The relaxation rates $R_{1,f}$, $R_{1,r}$, $R_{2,f}$, the fractional pool size F, and the exchange rate constants k_r and k_f are properties of tissue, and therefore to be fitted to data.

Chapitre 3

Methods

This chapter will present the methods employed in the work leading to this thesis and will be separated into two main sections. The first section will present all details about experimental methods in the initial validation of the *on-resonance* bSSFP model and the comparison between *on-* and *off-resonance* results. The second section will in turn present the motivation and design concept of the simulation and processing software package that emerged from this project.

3.1 Methods for *on-resonance* bSSFP validation

The validation of the *on-resonance* bSSFP method involves multiple steps. First, a numerical simulation is performed as initial validation of the model. Second, sensitivity tests are run to ensure the fitting is well conditioned and results reliable. Lastly, a simple comparison of *in vivo* data between the *on-resonance*

bSSFP model and the "gold-standard" *off-resonance* SPGR model is performed to access the variability of MT parameter values between these two methods. This section will provide a detailed explanation of the experimental methods employed in each step of this validation process.

3.1.1 Numerical simulation

The analytical solution presented is likely to deviate slightly from the steady-state reached by the Bloch differential equations due to assumptions that excitation, exchange and relaxation occur separately. As an initial validation step, a single voxel simulation is done by numerically solving the Bloch equations with variable sequence parameters. The result is then compared to the analytical solution. The standard ODE solver of Matlab (Version 2011b, MathWorks ®) is used to run through equations 2.29a-2.29d. The MT parameters and initial conditions are chosen from commonly reported values in literature, as reflected in Table 3–1 [15, 44].

TABLE 3–1: Table of MT parameters and initial conditions used in the numerical simulation of Bloch equations

MT parameters		initial conditions	
$T_{2,f} = 81\text{ms}$	$T_{2,r} = 12\mu\text{s}$	$M_{x,f} = 0$	$M_{z,f} = 1$
$F = 0.157$	$k_f = 4.45\text{s}^{-1}$	$M_{y,f} = 0$	$M_{z,r} = F$

One extra parameter needed to perform numerial simulations is the value of the absorption *lineshape on-resonance*. Because a *Super-Lorentzian* is not defined at $\Delta = 0$, an interpolation was performed and it agreed with the literature value of $G(0) = 1.4 \times 10^{-5}$ [15].

T_{RF} and α are the two sequence parameters to be varied separately during the simulation. Values of these two parameters were chosen as the following :

– T_{RF}(ms) : 0.23 to 1.84, in increments of 0.23, while fixing α at 35 degrees ;

– α(degrees) : 5, then 10 to 120 in increments of 10, while fixing T_{RF} at 0.23ms.

TR is 4ms for a T_{RF} of 0.23ms, and varies in such a way that TR $-$ T_{RF} is constant.

Three-lobe sinc pulses are used for the excitation. Once steady-state is reached, the magnitude of each component of the magnetization from this simulated voxel is sampled midway between two RF pulses, i.e. the echo time is $TE = \frac{\mathrm{TR}}{2}$. Fig. 3–1 shows a sequence of two sinc pulses. The pulses are alternated in a sequence, i.e. a pulse in the $+x'-$ direction (causing a *flip angle* of $+\alpha$) is always followed by a pulse in the $-x'$ direction (causing a *flip angle* of $-\alpha$). The application of alternating pulses allows steady-state to be reached much faster (in about 150 TR's).

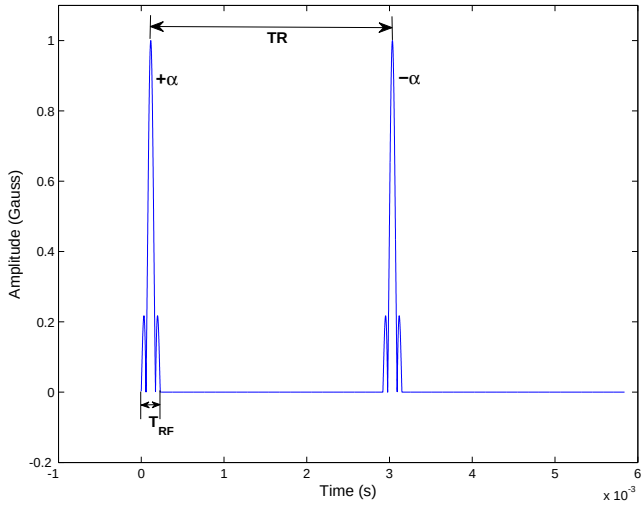

FIGURE 3–1: Illustration of alternating three-lobe sinc pulses used in the numerical simulation ($\alpha = 35^o$).

Since T_{RF} are very short and the ODE solver in Matlab (Version 2011b, MathWorks®) does not use fixed temporal steps, each TR is manually divided into 100 equal time increments to improve the accuracy in the simulation of the excitation pulse.

The results of the numerical simulation are then fitted to the analytical solution, using a least-square minimizing routine to extract the MT parameters. The fitted parameters are then compared to the original values used as a validation metric.

3.1.2 Sensitivity tests

Sensitivity tests of the analytical solution are performed to ensure parameter fitting is well-conditioned at a given range of sequence parameter values. The analytic solution is computed while varying individually each MT parameter between 90% to 110% of the reference value reported in Table 3–1, and plotted over the range of simulated sequence parameters. The plots are then visually inspected to identify the range of sequence parameters optimal for fitting.

3.1.3 Comparison of *on-resonance* bSSFP and *off-resonance* MT-SPGR *in vivo*

The standard bSSFP sequence has been modified to allow user-defined *flip angle* and T_{RF}, and implemented on a Siemens® Trio Tim 3T MRI scanner. The imaging protocol used for the *on-resonance* bSSFP sequence combines 8 images by varying α and 5 by varying the TR, as listed in Table 3–2. The *off-resonance* MT-SPGR sequence has been previously implemented on the Siemens machine using an optimized 10-point protocol [29]. Both *on-resonance* and *off-resonance* qMT images are acquired axially at a resolution of $2\times2\times2$mm isotropic with a matrix of 128-by-128 and 72 slices. The total imaging time for the *on-resonance* protocol is

around 10 minutes, whereas the total imaging time for the *off-resonance* protocol is nearly 50 minutes.

TABLE 3–2: Imaging protocol parameters used for the *on-resonance* bSSFP sequence

	Varying α	varying TR
α	5, 10, 12, 14, 16, 18, 20, 23	22
T_{RF} (μs)	300	300, 400, 500, 600, 800
TR(ms)	3.14	3.14, 3.24, 3.34, 3.44, 3.64

The R_1 values are separately obtained using T1-mapping by a standard Lock-Locker protocol using the same geometry as the qMT sequences [31]. The parameters F, k_f and $T_{2,r}$ are extracted by fitting each set of data to their respective model. Values of these parameters from both methods are then compared by simple regression.

3.2 Software development

QMT processing is in dire need of standardization. Existing processing pipelines only deal with fixed imaging protocols. As a result, image series numbers and protocol parameters are often hard-coded. Each slight modification in the imaging protocol requires manual overwriting of the pipeline code. A standardized processing software capable of handling data from different imaging protocols is needed. Furthermore, the idea of a user-friendly simulator for the *on-resonance* bSSFP

sequence would avoid manual set-ups of variable parameters and accelerate the simulation process.

Based on these needs, a standardized qMT simulation/processing software package is developed with the following design requirements :

– Include a graphical user interface (GUI) based simulator for the *on-resonance* bSSFP model, allowing for numerical simulation as well as visualization of the analytical solution.
– Include a GUI based data processing kit for the *off-resonance* SPGR method that handles common imaging protocols for this model. Base the fitting algorithm on the existing pipeline, while rebuilding the data-handling function.
– Allow possible extension of the simulator to include the *off-resonance* SPGR method as well.
– Allow a possible extension of the data processing kit to include customized *off-resonance* SPGR protocols, as well as the *on-resonance* bSSFP model.

The software package is built in Matlab (Version 2011b, MathWorks®), using the GUIDE toolkit to design the GUI. For existing data processing algorithms built using other platforms, a shell is written to ensure that all user interactions can be achieved in Matlab.

Chapitre 4

Results

This chapter will again be divided into two main sections. The first section will present results from the validation study of the *on-resonance* bSSFP model, including results from numerical simulation, sensitivity tests and *in vivo* comparison between *on-* and *off-resonance* methods. The second one will demonstrate the final product of the simulator/processing software package, detailing its functionality and features and presenting the validation results.

4.1 *On-resonance* bSSFP model validation

4.1.1 Numerical simulation

Simulation of the *on-resonance* bSSFP model is performed by numerically solving the coupled Bloch equations 2.29a-2.29d using the parameter values shown

in Table 3–1. A typical simulation of a single-voxel data with high temporal resolution of 500 steps per TR takes approximately 15 minutes to run. The result of this numerical simulation is then fitted to the analytical solution to extract the parameters.

Two different fitting routines are used. The fit first used *fminsearch* and then changed to *lsqnonlin* for the faster processing time and compatibility with parallel processing. The final routine with *lsqnonlin* is capable of fitting the analytical solution to a typical single-voxel data set of 13 data points within 5 seconds. Both fitting routines resulted in identical fits. The resulting fits with residuals are shown in Fig. 4–1. Note that although presented on different graphs, data from varying α and from varying T_{RF} are concatenated together for the fitting.

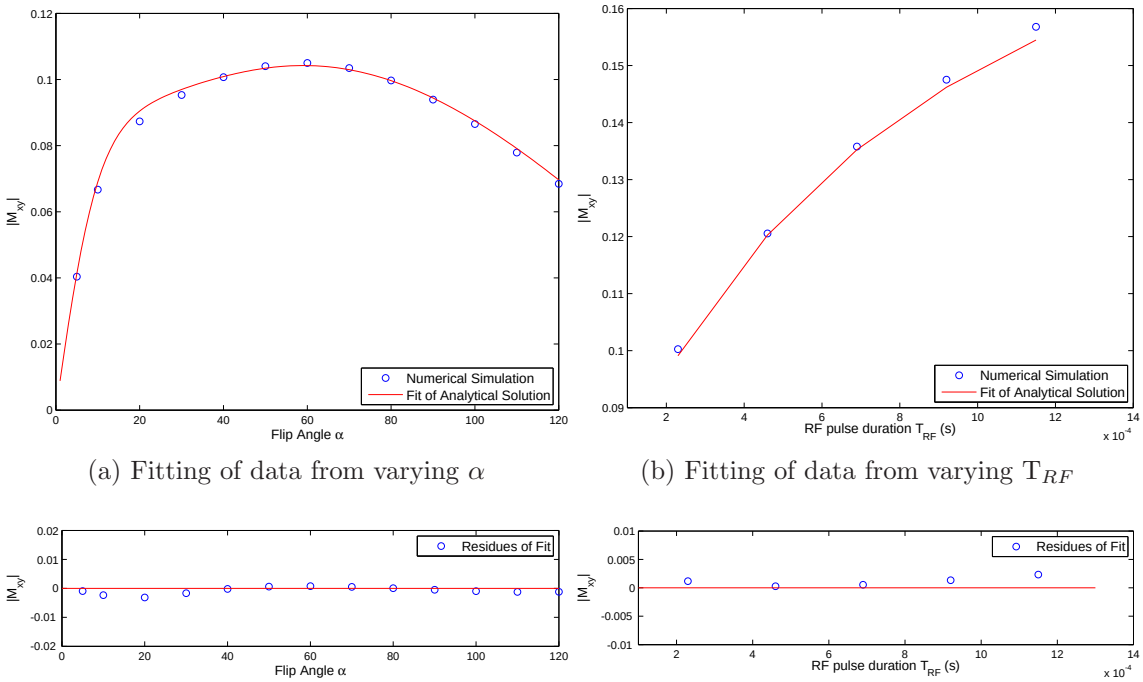

(a) Fitting of data from varying α

(b) Fitting of data from varying T_{RF}

(c) Residual

(d) Residual

FIGURE 4–1: Fitting of *on-resonance* data simulated by varying α and T_{RF} to the analytical solution, with residuals

As shown in Fig. 4–1, deviation of the fitted solution is within 2% of the simulated data. A comparison between the initial values of F and k_f and the values extracted from fitting are presented in Table 4–1.

TABLE 4–1: Comparison between parameters extracted from fit and parameters used in numerical simulation.

	Fitted	Used in numerical simulation	% Difference
$T_{2,f}$	81.3 ms	81 ms	0.4
F	0.1569	0.157	-0.07
k_f	4.73 s^{-1}	4.45 s^{-1}	6

Again the fitted values of the parameters agree with the original values used for the numerical simulation. The percent difference is slightly higher (6%) for k_f, the reason and impact of this will be discussed in Chapter 5.

4.1.2 Sensitivity tests

Sensitivity analysis of each parameter is done using the methods outlined in Section 3.1.2. Graphs of sensitivity tests of F, k_f, $T_{1,f}$ and $T_{2,f}$ are shown in Fig. 4–2.

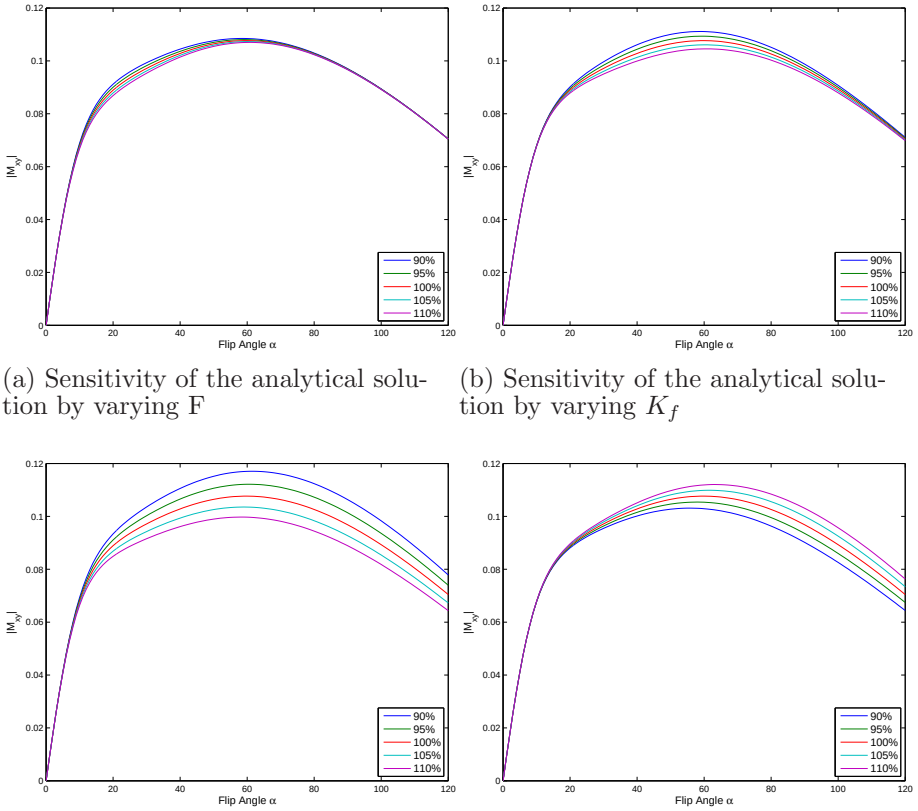

(a) Sensitivity of the analytical solution by varying F

(b) Sensitivity of the analytical solution by varying K_f

(c) Sensitivity of the analytical solution by varying $T_{1,f}$

(d) Sensitivity of the analytical solution by varying $T_{2,f}$

FIGURE 4–2: Sensitivity of the analytical solution by varying each parameter from 90% to 110% of its simulated value, while keeping other parameters constant.

As shown in Fig. 4–2, the analytical solution is sensitive to each parameter at different ranges of α. It is noticeable that the sensitivity regions for $T_{1,f}$, $T_{2,f}$ and k_f are similar, while the sensitivity to $T_{1,f}$ is significantly more pronounced.

4.1.3 Comparison of *in vivo* results between *on-resonance* bSSFP and *off-resonance* qMT-SPGR

In vivo images of both *on-resonance* bSSFP and *off-resonance* qMT-SPGR protocols outlined in Section 3.1.3 were acquired on a healthy male volunteer. Parameter maps for F and k_f are computed by fitting the data to their respective model. These maps are shown side-by-side for visual comparison, as shown in Fig. 4–3.

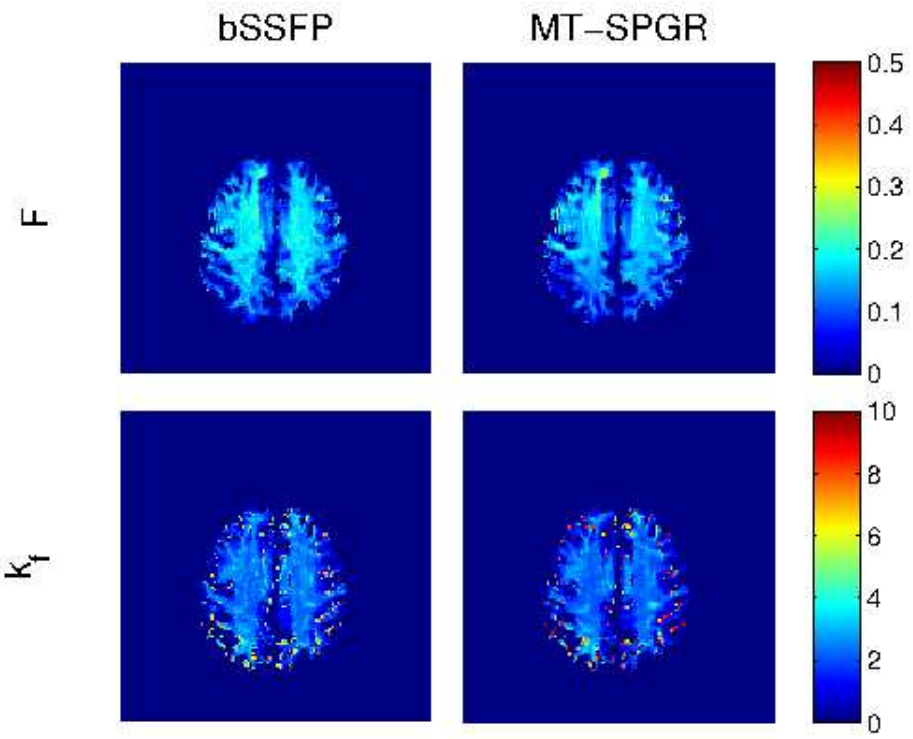

FIGURE 4–3: Comparison of F and k_f parameter maps extracted from *on-resonance* bSSFP, acquired in 10 minutes and *off-resonance* SPGR data, acquired in 50 minutes

As shown in Fig. 4–3, the two methods produce parameters in the same range of values. However, it is quite obvious that the two models have differences in the robustness of extracting each parameter. The *on-resonance* bSSFP method introduced more noise in the F map, whereas the *off-resonance* qMT-SPGR fit seems less stable with the k_f fit. The causes and impacts of these limitations in the two models will be further discussed in the next chapter.

A more detailed analysis of the parameter F is carried out, since studies have shown that F is correlated with the myelin content in brain tissue [9, 15]. F values in the chosen slice are plotted in a scatter plot as shown in Fig. 4–4. These points give a high coefficient of correlation $R = 0.925$. For the k_f values, although the simple correlation yields similar R value, more detailed analysis is not carried out for practical reasons, which will be further discussed in section 5.1.

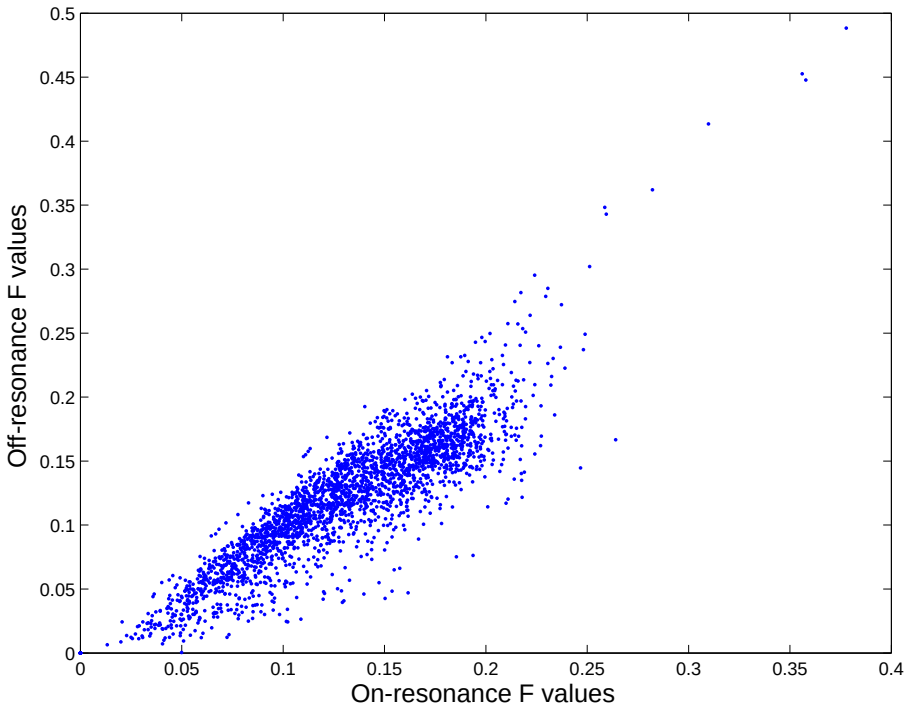

FIGURE 4–4: Scatter plot for comparison between F values from *on-resonance* bSSFP and *off-resonance* SPGR data from a randomly selected slice.

Two regions of interests (ROIs) are manually segmented for general WM and GM. The mean F values in each of the two ROIs for both models are listed in Table 4–2 below. It is worth noticing that these value are slightly higher than the literature reported values. This over-estimation can be accounted for by the type of $T1$ estimation method used, the details of which will be described in the next chapter.

TABLE 4–2: Comparison between mean F values from *on-resonance* bSSFP and *off-resonance* SPGR data found in each ROI

	on-resonance bSSFP	*off-resonance* SPGR	estimate from literature [15]
WM	0.197 ± 0.02	0.190 ± 0.01	0.157
GM	0.089 ± 0.002	0.099 ± 0.006	0.064

4.2 Final product of software package

The final product of the qMT software package consists of two main GUI based programs. The first one is a simulation tool that will assist users to have a better understanding of the behaviour of the *on-resonance* bSSFP model. This program in itself has three sub-applications : numerical simulator, sensitivity tester and single-voxel data fitting tool ; details of each application will be presented in section 4.2.1. The second program in this package is a data processing toolkit, designed to handle generalized protocols of the *off-resonance* qMT-SPGR method. Its functionality and features will be described in section 4.3.

4.2.1 Simulation tools for the *on-resonance* bSSFP model

This simulation tool is a Matlab (MathWorks®) based, GUI controlled simulation toolkit built in conjunction with the validation process of the *on-resonance* bSSFP method. A beta version was made publicly available and presented in August 2011, at the *ISMRM White Matter Study Group International Workshop on*

Advanced White Matter Imaging in Reykjavik, Iceland. The simulation tool kit is wrapped by a simple three-button interface to allow users to choose one of the three applications described in this section.

4.2.2 Numerical simulator

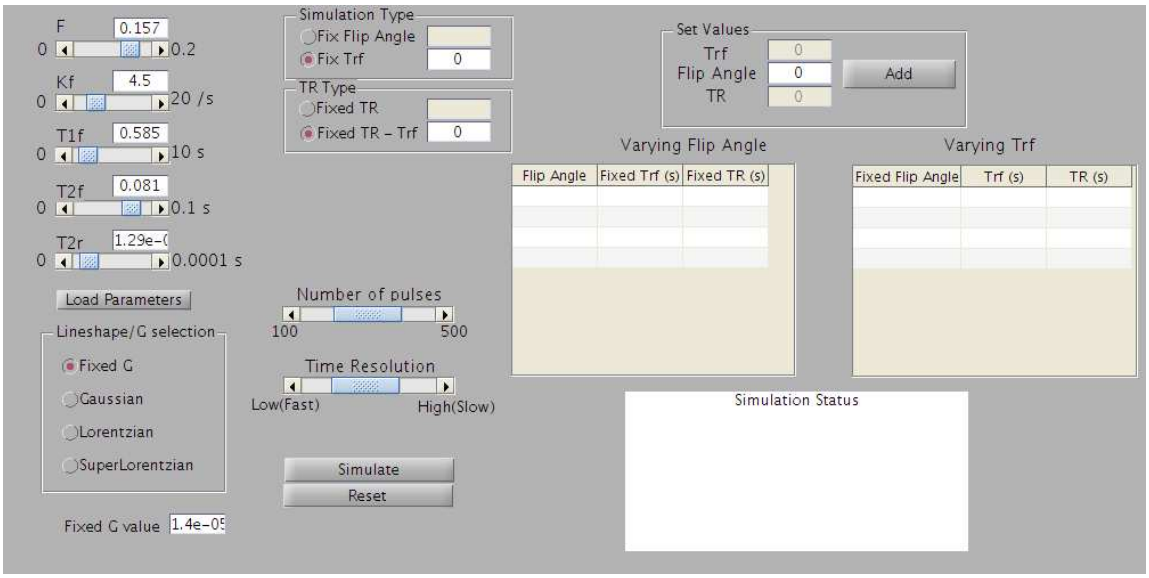

FIGURE 4–5: Screen-shot of the numerical simulator's graphical user interface

The numerical simulator, as shown in Fig. 4–5, allows users to set up a custom set of protocol parameters of the *on-resonance* bSSFP method and perform a numerical simulation of the Bloch equations using these parameters. Slide-bars and text fields allow quick choice of MT parameters to use during the simulation, while default values based on literature are loaded upon start-up. The protocol

parameters can be chosen by varying the *flip angle* and/or varying the RF pulse duration. Extra slide bars allow users to chose the number of pulses and time resolution for the simulation, giving users the freedom to decide on the trade-off between accuracy and running time. The simulated data are automatically saved. The protocol used to simulate can also be saved and loaded for future uses.

4.2.3 Sensitivity tester

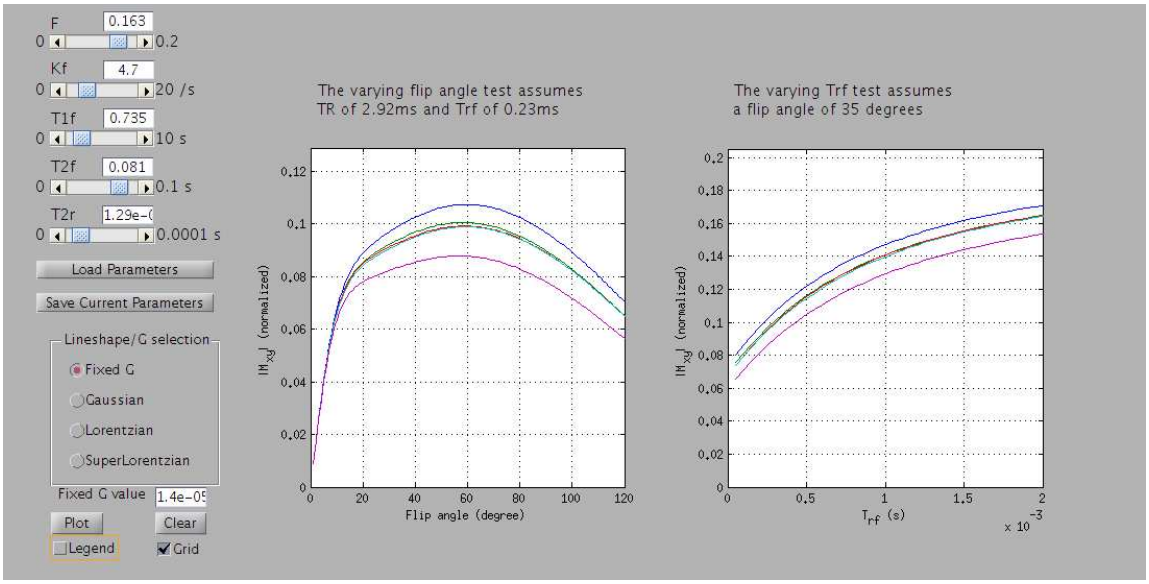

FIGURE 4–6: Screen-shot of the sensitivity tester's graphical user interface

The sensitivity tester, as shown in Fig. 4–6, allows users to quickly visualize the behaviour of the analytical solution of the bSSFP model based on different MT parameter values. Again, slide-bars and text fields allow quick setting of the MT

parameters. All previous plots are kept in the visualization area for comparison and can be erased quickly to clear the area. A check-box allows users to quickly turn on and off the legend in order to see all parameters used while not hiding the actual plots.

4.2.4 Single-voxel fitting tool

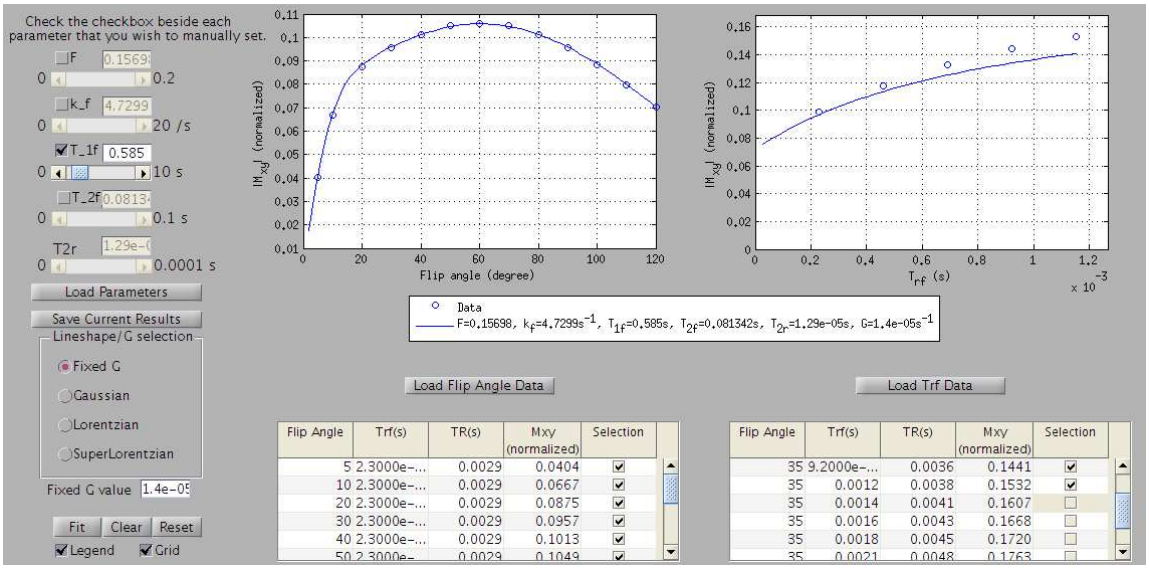

FIGURE 4–7: Screen-shot of the fitting tool's graphical user interface

This fitting tool allows users to perform the fitting of a simulated data point equivalent to a single-voxel data. Quick load buttons allow users to load simulated data or actual single-voxel data saved previously. The loaded data are listed in the data table, and featured check-boxes allow users to select the data points to use

in the fitting. This feature allows users to quickly see the influence of one or more data points on the fitting results. Extra check-boxes for the MT parameters - on top of slide-bars and text boxes - allow users to choose which parameters to fixed and which ones to fit for. Users will be able to take advantage of this feature to estimate to what extent each MT parameter influences the fitting.

4.2.5 Compatibility and stability

With the exception of variable window size and appearance on different operating systems, this software toolkit is stable and consistent based on extensive testing on different platforms and versions of Matlab (MathWorks®). The three parts of this toolkit are designed to be compatible with each other. Choices of MT parameters, simulated data as well as choices of *lineshapes* can be saved in one application and easily loaded in another.

4.3 Processing interface for *off-resonance* qMT-SPGR data

This processing interface is a GUI based Matlab (MathWorks®) software package built to facilitate data preparation and processing for the fitting of the *off-resonance* qMT-SPGR data. This package acts as a shell over the existing fitting pipeline to avoid manual definitions of file paths, protocol parameters and

acquisition numbers from a given set of acquired data. The user interface for this package is shown in Fig. 4–8.

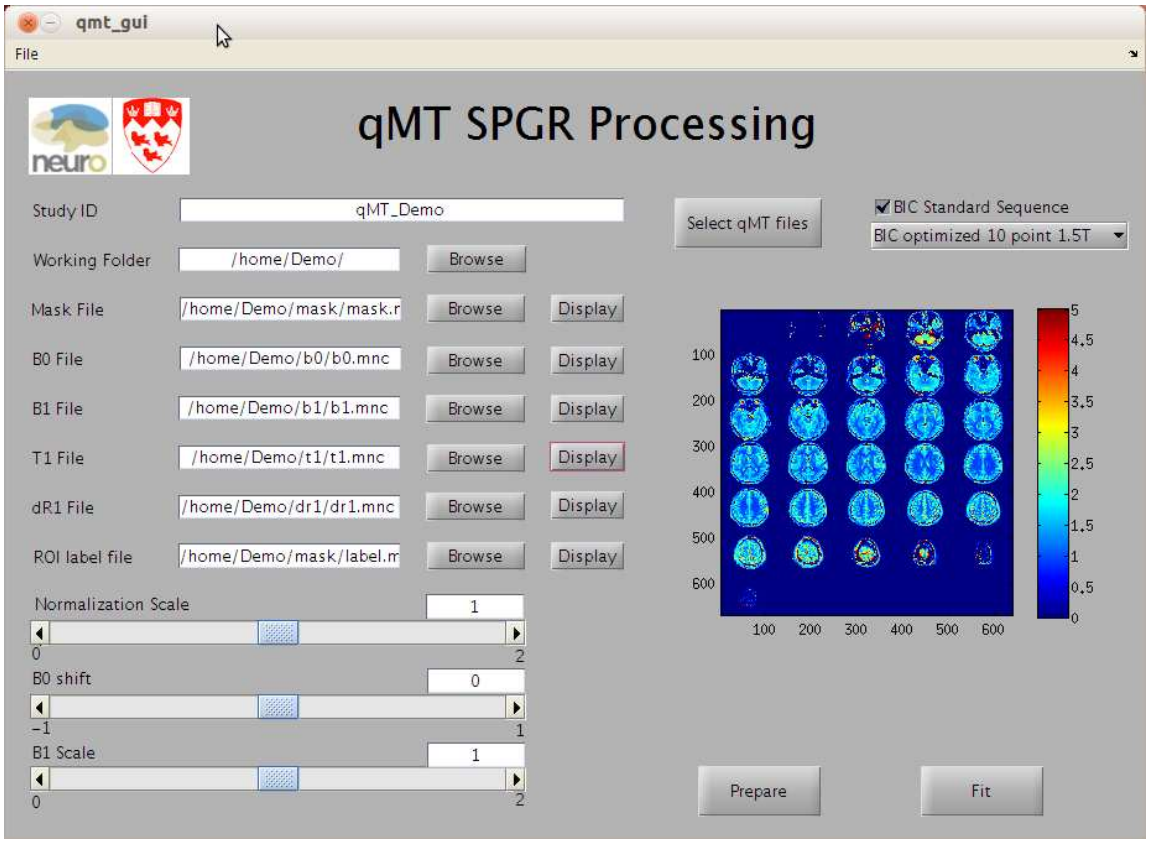

FIGURE 4–8: Screen shot of the data preparation and processing interface for the fitting pipeline of the *off-resonance* qMT-SPGR data

As shown in Fig. 4–8, this interface allows users to quickly choose pre-processed maps required for the fitting routine by clicking on browse buttons and choosing from UI windows. The interface also automatically fills the file paths for these files according to the most common naming convention once the working folder is

chosen, saving user's time from loading each one individually. The Display buttons allow users to instantaneously examine masked maps to ensure the use of correct files.

The images can be loaded using the **Select qMT files** button. Users are allowed to choose from pre-converted Minc files or convert from DICOM files. Once chosen, users can use the up/down button to sort these files according to the order used in the imaging protocol. The files are automatically sorted if a standard imaging protocol is used.

Once all necessary files are properly loaded, a prepare button allows users to perform a quick ROI fit of the data and visualize the result in a matter of a few seconds. This feature is added for two purposes : (i)-to allow users to make a last check on the data structure before launching the long fitting process ; and (ii)-to allow users to adjust the normalization and scaling factors, if necessary, based on the initial ROI fit.

The actual fitting can be then launched, with an option to divide the task in multiple segments that can be simultaneously submitted to a server, in order to save processing time. This feature is possible since the fitting is done voxel-wise and can be performed on any number of voxels in the data set.

Save/load menu options allow users to save naming conventions and protocol settings of frequently repeated protocols and facilitate future use.

Chapitre 5

Discussion

Chapter 4 presented results from the initial validation of the new *on-resonance* bSSFP method for qMT imaging and introduced the software package that emerged in the process. The initial validation showed good reproducibility of the *on-resonance* bSSFP method and good agreement with the "gold-standard" *off-resonance* SPGR method in estimating the value of the fractional pool size F. The software package also promises to be useful and practical for future studies in this subject matter. However, several issues also arose from the validation and needed to be resolved. Additionally, many possible extensions can be implemented to the software package to produce a more complete and general tool for qMT analysis. The first section of this chapter will address the issues related to the validation process of the *on-resonance* bSSFP method. This will include an assessment of

the over-estimation between simulated and fitted values for the parameter k_f, a discussion about the conditioning of the fits and an explanation about the consistently high value of F in *in vivo* data. This will be followed by a section focusing on the software package, assessing its potential uses and ways to expand the package.

5.1 Issues in the validation of *on-resonance* bSSFP

The first issue encountered during the validation process is the slight over-estimation between the value of k_f from fitting the simulated data to the analytical solution, and the true value of k_f used for the simulation. Beside the sensitivity of the k_f parameter itself, this difference is caused by one key simplification of the *on-resonance* bSSFP model : the assumption of instantaneous excitation [15]. This assumption does not take into consideration the relaxation and exchange taking place during the excitation itself. For very short durations of the RF pulse, instantaneous excitation is a good approximation to the true physical behaviour of the system. Although bSSFP sequences can have very short RF pulse durations, longer T_{RF}'s must be included to get a reasonable range of controlled variables. As shown in Fig. 4–1, only the five shortest values - instead of all 8 used for the numerical simulation - are used for the fitting. The data for the fifth shortest T_{RF}

is already underestimated by the analytical solution, and the solution tends to further underestimate the real value of the transverse magnetization for longer T_{RF}, as expected. While this issue can be theoretically avoided by using very short T_{RF}, hardware limitations prevent the implementation of such pulses.

The original study was performed at 1.5T, so SAR was not an issue. It did become an issue during the validation on the 3T MRI. Because of its very short RF pulse duration, the amplitude of the RF pulse has to be increased to achieve the desired *flip angle*. Therefore the power deposition increases significantly. For an RF pulse short enough to give an accurate approximation, the *flip angle* is limited by SAR to below 20 degrees. From the sensitivity analysis results presented in Section 4.1.2, the fitting is most sensitive to F for *flip angle*s between 15° to 50° and to k_f for *flip angle*s between 20° to 70°. Using only *flip angle*s below 20° will cause the fitting to be unreliable. Longer pulse durations are needed to acquire sample points at higher *flip angle*. This causes a trade-off between accuracy of the approximation and the sensitivity of the fitting. More in depth analysis is needed to fully assess the fitting behaviour and optimize the imaging protocol. Gloor *et al.* also proposed a *non-balanced SSFP* model that takes into consideration the relaxation and transfer happening during the excitation stage. The validation and

sensitivity analysis of such model would be a good candidate for future works as a continuation of this thesis. [16]

The sensitivity analysis results presented in Section 4.1.2 also suggest that the analytical solution is significantly more sensitive to $T_{1,f}$ than to other parameters. This issue can be easily addressed by extracting $T_{1,f}$ maps using existing T_1 mapping techniques such as Look-Locker or varible flip-angle (VFA) [30, 37, 49]. However, recent studies have shown that biases exist between different techniques of T_1 estimation [3, 46]. This bias extends to the qMT models since T_1 maps are necessary in the fitting of the qMT data. The assessment of the extent to which variations in estimated T_1 values influence the qMT parameter estimation is still a work in progress [46]. However, this will likely account for the over-estimation of the experimental values of F compared to literature values mentioned in Section 4.1.3.

Another issue related to the *in vivo* comparison between *on-resonance* bSSFP and *off-resonance* SPGR is the different behaviour of the fitting routine with respect to different parameters. As mentioned in Section 4.1.3, the *on-resonance* bSSFP fitting results in noisier F maps, whereas the *off-resonance* SPGR fitting results in more noise in the k_f map. From the sensitivity analysis, it is obvious that these two parameters have competing effects during the fit. More in depth examination

of the parameter sensitivities using the simulation software reveals that for lower values of F the model's sensitivity to both F and k_f becomes very low, resulting in a poorly conditioned fit. Since F has been shown to correlate with myelin content and no direct relation between k_f and tissue properties has been found, for practicality, F should be favoured in the fitting. The optimized *off-resonance* SPGR fitting routine does include a process that favours the correct estimation of F at the expense of inaccuracy in k_f. However, the current *on-resonance* bSSFP fitting routine does not favour one parameter over another. From the result it is clear that the estimation of F is noisier with the *on-resonance* bSSFP fitting routine.

5.2 Extensions for software package

The qMT software developed for this project has great potential for use in future qMT studies. However, the functionality of this package is not limited to the extent this project. One strong feature of the initial design idea is the open possibility for extensions, the most important one being customizable protocol parameters. The data structures of this package separates the imaging protocol from the acquired data, which allows users to easily build and save customized

protocol parameters and share it with others. This feature provides the possibility to generalize the data processing to all qMT protocols.

Other possible extensions to the package - proposed in the original design idea but not fully implemented yet - include the expansion of the simulation kit to include *off-resonance* models, and the inclusion of pre-processing functions in the data processing interface. This, of course, requires a collaborative effort with other software developers that have designed pre-processing modules.

Chapitre 6

Conclusion and future works

6.1 Conclusion

This thesis presented the initial validation of the newly developed balanced steady-state free precession model for quantitative magnetization transfer imaging. It also introduced a software package for standardized qMT data processing. The objectives were to investigate the underlying mechanism of the *on-resonance* bSSFP method, assess its reliability and compare it to the existing *off-resonance* spoiled-gradient method for qMT imaging. With the development of the software package, this thesis also contributes to deeper understanding of qMT mechanisms in general. Numerical simulation, sensitivity analysis and *in vivo* comparison between the two models were performed. A GUI based simulator and processing interface are implemented in Matlab (MathWorks®).

Numerical simulation and sensitivity tests showed good predictive power of the analytical solution and excellent reproducibility using the analytical model in the normal range of parameters. Although the instantaneous excitation assumption leads to slight underestimation by the analytical model for longer RF pulse durations, the model proves to be robust for optimal values of T_{RF}. Initial validation by comparison of *in vivo* results between the *on-resonance* bSSFP and the *off-resonance* SPGR methods showed agreement. Explanations are provided for the discrepancy between general experimental results and literature values. This initial validation confirms that the *on-resonance* bSSFP method is valid for the purposes of qMT imaging, though additional fine-tuning and optimization are needed to make it as robust as the "gold-standard" *off-resonance* SPGR method in the presence of noise and other biasing factors.

Much work remains to be done to fully validate, optimize and implement the *on-resonance* bSSFP method for qMT imaging purposes. A starting point would be a potential modification of the analytical solution to account for non-instantaneous excitation pulses. This could be achieved by breaking the RF pulse duration into multiple shorter periods of instantaneous excitation followed by free precession, in order to give more accurate modelling of the longer duration RF pulses. Other tasks include the choice of optimal imaging protocols, the development of a robust

fitting routine favouring the correct estimation of F, and assessment of the impact of T_1 estimation bias on the result. With its promising properties such as high signal-to-noise ratio and especially short scan time, this *on-resonance* bSSFP method has an advantage over the existing *off-resonance* SPGR sequences in terms of clinical practicality. Further investigation of this model is an important direction for future work.

Additionally, a qMT software package was developed to accompany the validation project. The package facilitated, from a technical perspective, the validation process, and offered insights for better understanding of the underlying mechanisms. Part of the package was presented to the qMT imaging community and made publicly available to provide assistance in other qMT imaging studies. Many possible extensions have been proposed for the package, as discussed in Section 5.2, in the effort to make it a complete and general software useful to the entire qMT imaging community.

This thesis provides a framework for standardizing the validation and fitting of qMT data. The software package is made freely available to the MR community and is expected to become an indispensable tool for future qMT studies, leading the way toward fast, robust and clinically feasible qMT protocols.

References

[1] Alonso Ortiz, E. Quantitative functional mri based evaluation of caffeines effects on brain physiology. Master's thesis, McGill University, 2011.

[2] Bangerter, N. K., Hargreaves, B. A., Vasanawala, S. S., Pauly, J. M., Gold, G. E., and Nishimura, D. G. Analysis of multiple-acquisition ssfp. *Magnetic Resonance in Medicine 51*, 5 (2004), 1038–1047.

[3] Barral, J. K., Gudmundson, E., Stikov, N., Etezadi-Amoli, M., Stoica, P., and Nishimura, D. G. A robust methodology for in vivo t1 mapping. *Magnetic Resonance in Medicine 64*, 4 (2010), 1057–1067.

[4] Bieri, O., and Scheffler, K. On the origin of apparent low tissue signals in balanced ssfp. *Magnetic Resonance in Medicine 56*, 5 (2006), 1067–1074.

[5] Bieri, O., and Scheffler, K. Optimized balanced steady-state free precession magnetization transfer imaging. *Magnetic Resonance in Medicine 58*, 3 (2007), 511–518.

[6] Bloch, F. Nuclear induction. *Physical Review 70*, 7-8 (1946), 460–474.

[7] Carr, H. Y. Steady-state free precession in nuclear magnetic resonance. *Phys. Rev. 112* (Dec 1958), 1693–1701.

[8] Crooijmans, H. J., Gloor, M., Bieri, O., and Scheffler, K. Influence of mt effects on t2 quantification with 3d balanced steady-state free precession imaging. *Magnetic Resonance in Medicine 65*, 1 (2011), 195–201.

[9] Davies, G. R., Ramani, A., Dalton, C. M., Tozer, D. J., Wheeler-Kingshott, C. A., Barker, G. J., Thompson, A. J., Miller, D. H., and Tofts, P. S. Preliminary magnetic resonance study of the macromolecular proton fraction in white matter : a potential marker of myelin ? *Multiple Sclerosis 9*, 3 (2003), 246–249.

[10] Edzes, H. T., and Samulski, E. T. The measurement of cross-relaxation effects in the proton {NMR} spin-lattice relaxation of water in biological

systems : Hydrated collagen and muscle. *Journal of Magnetic Resonance (1969) 31*, 2 (1978), 207 – 229.

[11] Garcia, M., Gloor, M., Bieri, O., Wetzel, S., Radue, E.-W., and Scheffler, K. Mtr variations in normal adult brain structures using balanced steady-state free precession. *Neuroradiology 53*, 3 (2011), 159–167.

[12] Garcia, M., Gloor, M., Radue, E.-W., Stippich, C., Wetzel, S., Scheffler, K., and Bieri, O. Fast high-resolution brain imaging with balanced ssfp : Interpretation of quantitative magnetization transfer towards simple mtr. *NeuroImage 59*, 1 (2012), 202 – 211.

[13] Garcia, M., Gloor, M., Wetzel, S., Radue, E.-W., Scheffler, K., and Bieri, O. Characterization of normal appearing brain structures using high-resolution quantitative magnetization transfer steady-state free precession imaging. *NeuroImage 52*, 2 (2010), 532 – 537.

[14] Gloor, M. *Magnetization Transfer Imaging Using Steady-state Free Precession MR Sequences*. PhD thesis, University of Basel, 2010.

[15] Gloor, M., Scheffler, K., and Bieri, O. Quantitative magnetization transfer imaging using balanced ssfp. *Magnetic Resonance in Medicine 60*, 3 (2008), 691–700.

[16] Gloor, M., Scheffler, K., and Bieri, O. Nonbalanced ssfp-based quantitative magnetization transfer imaging. *Magnetic Resonance in Medicine 64*, 1 (2010), 149–156.

[17] Graham, S. J., and Henkelman, R. M. Understanding pulsed magnetization transfer. *Journal of Magnetic Resonance Imaging 7*, 5 (1997), 903–912.

[18] Haacke, E., Brown, R., Thompson, M., and Venkatesan, R. *Magnetic Resonance Imaging : Physical Principles and Sequence Design*. Wiley, 1999.

[19] Henkelman, R., Stanisz, G., and Graham, S. Magnetization transfer in mri : a review. *NMR in Biomedicine 14*, 2 (2001), 57–64.

[20] Henkelman, R. M., Huang, X., Xiang, Q. S., Stanisz, G. J., Swanson, S. D., and Bronskill, M. J. Quantitative interpretation of magnetization transfer. *Magn Reson Med 29*, 6 (1993), 759–66.

[21] Kuperman, V. *Magnetic Resonance Imaging : Physical Principles and Applications*. Academic Press Series in Electromagnetism. Academic Press, 2000.

[22] Lauterbur, P. C. Image formation by induced local interactions : Examples employing nuclear magnetic resonance. *Nature 242*, 5394 (Mar. 1973), 190–191.

[23] Lazzarini, R. *Myelin Biology and Disorders*. Elsevier Academic Press, 2004.

[24] Levesque, I. *Quantitative magnetic resonance imaging of magnetization transfer and T2 relaxation in human white matter pathology*. PhD thesis, McGill University, 2009.

[25] Levesque, I., Stikov, N., Pike, B., and Pauly, J. Drift in the magnetization transfer signal : Effect on quantitative mt experiments. *Proceedings of the International Society for Magnetic Resonance in Medicine, Montreal, Canada* (2011), 2782.

[26] Levesque, I. R., Chia, C. L., and Pike, G. B. Reproducibility of in vivo magnetic resonance imagingbased measurement of myelin water. *Journal of Magnetic Resonance Imaging 32*, 1 (2010), 60–68.

[27] Levesque, I. R., Giacomini, P. S., Narayanan, S., Ribeiro, L. T., Sled, J. G., Arnold, D. L., and Pike, G. B. Quantitative magnetization transfer and myelin water imaging of the evolution of acute multiple sclerosis lesions. *Magnetic Resonance in Medicine 63*, 3 (2010), 633–640.

[28] Levesque, I. R., Sled, J. G., Narayanan, S., Giacomini, P. S., Ribeiro, L. T., Arnold, D. L., and Pike, G. B. Reproducibility of quantitative magnetization-transfer imaging parameters from repeated measurements. *Magnetic Resonance in Medicine 64*, 2 (2010), 391–400.

[29] Levesque, I. R., Sled, J. G., and Pike, G. B. Iterative optimization method for design of quantitative magnetization transfer imaging experiments. *Magnetic Resonance in Medicine 66*, 3 (2011), 635–643.

[30] Lin, W., and Song, H. Improved accuracy in t1 mapping and flip angle correction with random spoiling in radial gradient echo imaging. In *Proc. Intl. Soc. Mag. Reson. Med* (2009), vol. 17, p. 4440.

[31] Margaret Cheng, H.-L., Stikov, N., Ghugre, N. R., and Wright, G. A. Practical medical applications of quantitative mr relaxometry. *Journal of Magnetic Resonance Imaging 36*, 4 (2012), 805–824.

[32] McConnell, H. M. Reaction rates by nuclear magnetic resonance. *The Journal of Chemical Physics 28*, 3 (1958), 430–431.

[33] Miller, K. L., Tijssen, R. H., Stikov, N., and Okell, T. W. Steady-state mri : methods for neuroimaging. *Imaging 3*, 1 (2011), 93–105.

[34] Morrison, C., and Mark Henkelman, R. A model for magnetization transfer in tissues. *Magnetic Resonance in Medicine 33*, 4 (1995), 475–482.

[35] Nishimura, D. G. *Principles of Magnetic Resonance Imaging*. Stanford University, 1996.

[36] Nolte, J., and Sundsten, J. *The Human Brain : An Introduction to Its Functional Anatomy*. No. no. 798 in Human Brain. Mosby, Incorporated, 2002.

[37] Park, D. J., Bangerter, N. K., Javed, A., Kaggie, J., Khalighi, M. M., and Morrell, G. R. A statistical analysis of the blochsiegert b 1 mapping technique. *Physics in Medicine and Biology 58*, 16 (2013), 5673.

[38] Pike, G. B. Pulsed magnetization transfer contrast in gradient echo imaging : A two-pool analytic description of signal response. *Magnetic Resonance in Medicine 36*, 1 (1996), 95–103.

[39] Pike, G. B., De Stefano, N., Narayanan, S., Worsley, K. J., Pelletier, D., Francis, G. S., Antel, J. P., and Arnold, D. L. Multiple sclerosis : Magnetization transfer mr imaging of white matter before lesion appearance on t2-weighted images. *Radiology 215*, 3 (2000), 824–830.

[40] Purcell, E. M., Torrey, H. C., and Pound, R. V. Resonance absorption by nuclear magnetic moments in a solid. *Physical Review 69* (Jan. 1946), 37–38.

[41] Ropele, S., Strasser-Fuchs, S., Augustin, M., Stollberger, R., Enzinger, C., Hartung, H.-P., and Fazekas, F. A comparison of magnetization transfer ratio, magnetization transfer rate, and the native relaxation time of water protons related to relapsing-remitting multiple sclerosis. *American Journal of Neuroradiology 21*, 10 (2000), 1885–1891.

[42] Scheffler, K., and Lehnhardt, S. Principles and applications of balanced ssfp techniques. *European Radiology 13*, 11 (2003), 2409–2418.

[43] Sled, J. G., and Pike, G. Quantitative interpretation of magnetization transfer in spoiled gradient echo MRI sequences. *Journal of Magnetic Resonance 145*, 1 (2000), 24 – 36.

[44] Sled, J. G., and Pike, G. B. Quantitative imaging of magnetization transfer exchange and relaxation properties in vivo using mri. *Magnetic resonance in medicine 46*, 5 (2001), 923–931.

[45] Stikov, N. Cross-relaxation imaging : Methods, challenges and applications. *CONFERENCE ON MEDICAL PHYSICS AND BIOMEDICAL ENGINEERING* (2010), 7.

[46] Stikov, N. Improving the accuracy of cross-relaxation imaging. *International Journal of Imaging Systems and Technology 22*, 1 (2012), 67–72.

[47] Stikov, N., Cukur, T., Dougherty, R., Wandell, B., and Pauly, J. Sensitivity analysis of cross-relaxation imaging. *Proceedings of the International Society for Magnetic Resonance in Medicine 15th Annual Meeting, Berlin, Germany* (2007), 1805.

[48] Stikov, N., Keenan, K. E., Pauly, J. M., Smith, R. L., Dougherty, R. F., and Gold, G. E. Cross-relaxation imaging of human articular cartilage. *Magnetic Resonance in Medicine 66*, 3 (2011), 725–734.

[49] Tardif, C., Stikov, N., Levesque, I., and Pike, B. Impact of three b1 mapping techniques on variable flip angle t1 measurements. In *Proc ISMRM* (2011), vol. 19, p. 2745.

[50] Wolff, S. D., and Balaban, R. S. Magnetization transfer contrast mtc and tissue water proton relaxation in vivo. *Magnetic Resonance in Medicine 10*, 1 (1989), 135–144.

[51] Wu, X. Lineshape of magnetization transfer via cross relaxation. *Journal of Magnetic Resonance (1969) 94*, 1 (1991), 186 – 190.